行政院國家科學委員會專題研究計畫 成果報告

新型表面擇頻元件之設計：分析與計算(2/2)
研究成果報告(完整版)

計 畫 類 別 ：個別型
計 畫 編 號 ：NSC 95-2221-E-002-220-
執 行 期 間 ：95 年 08 月 01 日至 96 年 10 月 31 日
執 行 單 位 ：國立臺灣大學應用力學研究所

計 畫 主 持 人：陳瑞琳

計畫參與人員：博士班研究生-兼任助理：楊適壕
碩士班研究生-兼任助理：洪士哲

報 告 附 件 ：出席國際會議研究心得報告及發表論文

處 理 方 式 ：本計畫可公開查詢

中 華 民 國 96 年 09 月 13 日

行政院國家科學委員會補助專題研究計畫 ■ 成 果 報 告
□期中進度報告

新型表面擇頻元件之設計：分析與計算(2/2)

計畫類別：■ 個別型計畫　　□ 整合型計畫
計畫編號：NSC 95－2221－E－002－220
執行期間：2006/08/01 至 2007/10/30
計畫主持人：陳瑞琳
共同主持人：無
計畫參與人員：洪士哲、楊適壕

成果報告類型(依經費核定清單規定繳交)：□精簡報告　■完整報告

本成果報告包括以下應繳交之附件：
□赴國外出差或研習心得報告一份
□赴大陸地區出差或研習心得報告一份
□出席國際學術會議心得報告及發表之論文各一份
□國際合作研究計畫國外研究報告書一份

處理方式：除產學合作研究計畫、提升產業技術及人才培育研究計畫、列管計畫及下列情形者外，得立即公開查詢
□涉及專利或其他智慧財產權，□一年□二年後可公開查詢

執行單位：

中　華　民　國　九十六 年 九 月 十三 日

Table of Contents

Table of Figures

1 Introduction

Frequency selective surface (FSS), which is two-dimensional periodic structure, has widespread applications over much of electromagnetic spectrum because of its filtering property. In the microwave region, a FSS can make an reflector antennas more efficient, and in radome design, it provides bandpass transmission characteristic at the operator frequency of the antenna [1]. In the far-infrared region, a FSS is used as polarizers and beam splitter [2], and in infrared sensor, a FSS absorbs the desired frequencies in the substrate material backing the screen [2]. Recently, FSS realize the multiband artificial magnetic conducting (AMC) surface, known as metamaterial, improve antenna performances and reduce surface wave within the substrate[3]. The split ring resonators (SRR) proposed by Pendry *et al.* [4] were shown to exhibit strong magnetic response to the incident field. In the long wavelength limit, the effective permeability of the SRR structure can be negative. Therefore, SRR serve as the key element for a left handed composite medium where the permeability and permittivity are simultaneously negative.

Equivalent circuit model, mutual impedance approach and modal (integral) method are three major methods to analyze FSS. Here we use integral method and solve it by moment method. Simple is the benefit of equivalent circuit, but this method cannot handle arbitrary element shape and dielectric loading effects, and it is only accurate up to the resonant frequency of the screen. However, Ohira [5] purpose some equivalent circuit model to govern arbitrary shape FSS.

Patch and aperture type of FSS, element shape, size, lattice constant, dielectric, grating lobes and Wood's anomalies effect the transmission and reflection profiles of FSS.

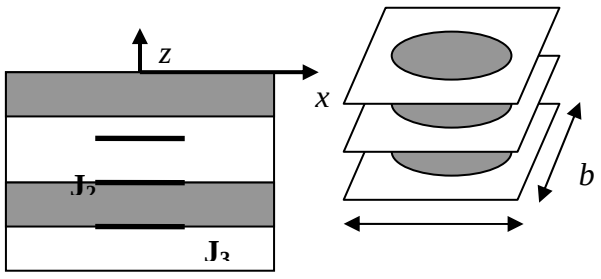

FIGURE 2.1 Multi-layered FSS

2 Formulation

The analysis of multi-layered FSS which is shown as Fig. 2.1 is that the monochromic incident wave propagates through dielectrics without conducting screen will produce the transmitted field and the reflected wave denoted by $\mathbf{E}^{inc}$. Moreover, the induced current $\mathbf{J}$ which comes from that incident field propagates the conducting screen produces scattered field $\mathbf{E}^{s}$.

Electric field integral equation (EFIE) can be obtained from Maxwell's equation and applying boundary condition that the transverse electric field $\mathbf{E}_t$ of conducting screen with finite conductivity is . We employ Floquet's theorem to discretize EFIE because of periodicity of FSS. Thus the operator equation is shown as

$$-\begin{bmatrix} E_{ix}^{inc} \\ E_{iy}^{inc} \end{bmatrix} = \sum_{j=1}^{M}\sum_{-\infty}^{\infty}\sum_{-\infty}^{\infty}\begin{bmatrix} \tilde{G}_{xx}^{ij} & \tilde{G}_{xy}^{ij} \\ \tilde{G}_{yx}^{ij} & \tilde{G}_{yy}^{ij} \end{bmatrix}\begin{bmatrix} \tilde{J}_{jx} \\ \tilde{J}_{jy} \end{bmatrix} e^{j(\alpha_m x+\beta_n y)} - R_s\begin{bmatrix} J_{ix} \\ J_{iy} \end{bmatrix}$$

and we apply spectral domain immitance approach [6] to obtain the spectral dyadic Green's function.

Using Galerkin approach of moment method with roof-top basis function, and applying fast Fourier's transform (FFT) for faster computation, we can get moment method equation

$$-\begin{bmatrix} E_{x0}\tilde{T}_{x,00}^{*}(0,0)P^{*}\left(p+\frac{1}{2},q\right) \\ E_{y0}\tilde{T}_{y,00}^{*}(0,0)P^{*}\left(p,q+\frac{1}{2}\right) \end{bmatrix} =$$

$$\begin{bmatrix} P^{*}(p,q) & 0 \\ 0 & P^{*}(p,q) \end{bmatrix}\cdot \mathrm{FFT}^{-1}\left\{\begin{bmatrix} \tilde{G}_{xx}^{'}(m,n) & \tilde{G}_{xy}^{'}(m,n) \\ \tilde{G}_{yx}^{'}(m,n) & \tilde{G}_{yy}^{'}(m,n) \end{bmatrix}\cdot \mathrm{FFT}\left\{\begin{bmatrix} P(p',q') & 0 \\ 0 & P(p',q') \end{bmatrix}\begin{bmatrix} I_x(p',q') \\ I_y(p',q') \end{bmatrix}\right\}_{mn}\right\}_{pq}$$

$$-R_s\begin{bmatrix} F_x(p,q) & 0 \\ 0 & F_y(p,q) \end{bmatrix}\begin{bmatrix} I_x(p,q) \\ I_y(p,q) \end{bmatrix}$$

Finally, we use conjugate gradient method to solve the amplitude of induced current.

3 Numerical Results

3.1 Patch and Aperture

At resonance, a patch-element freestanding FSS has total reflection, whereas an aperture-element freestanding FSS has total transmission, that is, a patch-element FSS is a bandstop filter while an aperture-element FSS is a bandpass filter.

If the conducting screen is perfect conductor, the thickness of the conducting screen is infinitely thin without dielectrics, from Babinet's principle, the reflection coefficient for patch equals the transmission coefficient as shown in FIGURE 3-1.The element shape is square with length equal to $4.06mm$ illuminated by the normally incident field polarized in y direction, the lattice constant for x and y direction both equal to $10mm$. A 32×32 grid is employed to discrete the unit cell.

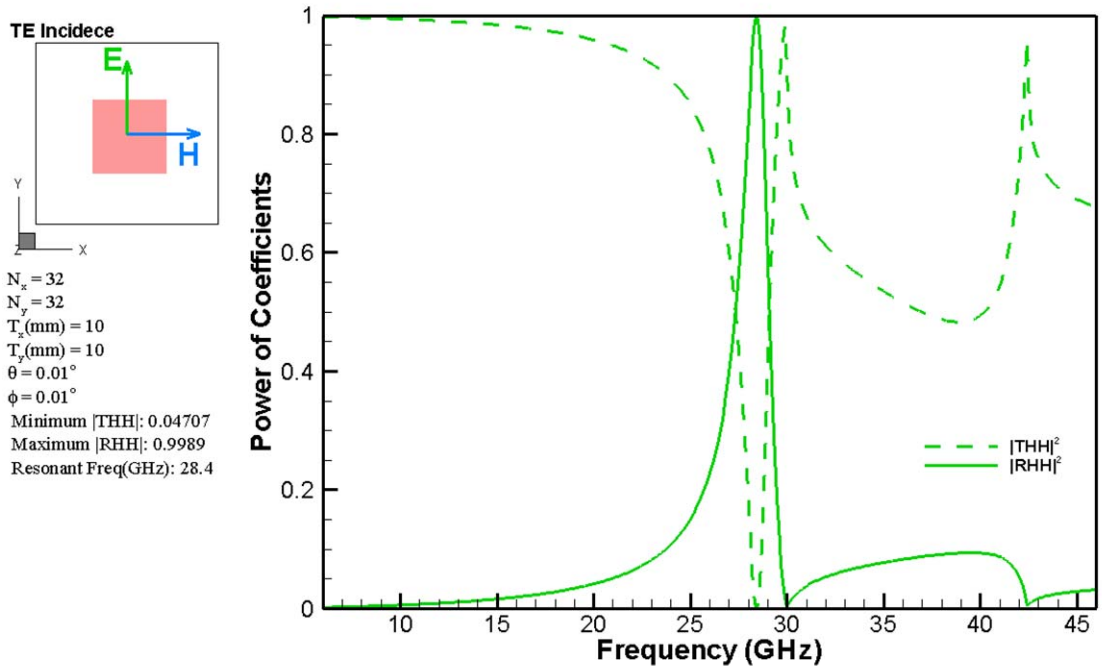

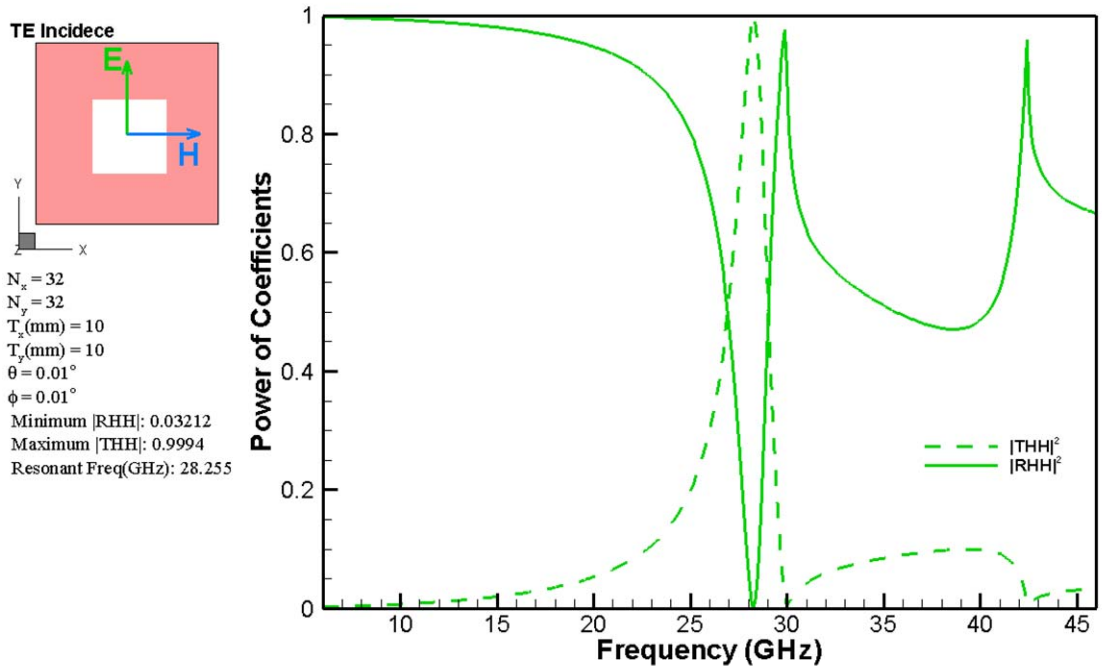

FIGURE 3-1 ***Top:*** periodic structure of patches. ***Bottom:*** periodic structure of apertures. The power of reflection coefficient for patch is equal to the power of transmission coefficient for aperture.

Next, consider the rectangle shape, the resonant wavelength λ_r of a single flat strip dipole without dielectrics of length L and width b as[7]

Equation Chapter 3 Section 1
$$\lambda_r = 2.1\left(1+\frac{d}{2L}\right)L \tag{3.1}$$

For a dipole with $L = 5mm$ and $d = 0.625mm$, λ_r should be $11.2mm$.In our calculation in FIGURE 3-2, λ_r is $11.6mm$.

As mentioned above, applying Babinet's principle, the resonant frequency of slot is equal to the resonant frequency of dipole, but the resonant frequency exists only that E-field parallels to length of dipole arrays, while H-field parallels to length of slot arrays as shown in FIGURE 3-3.

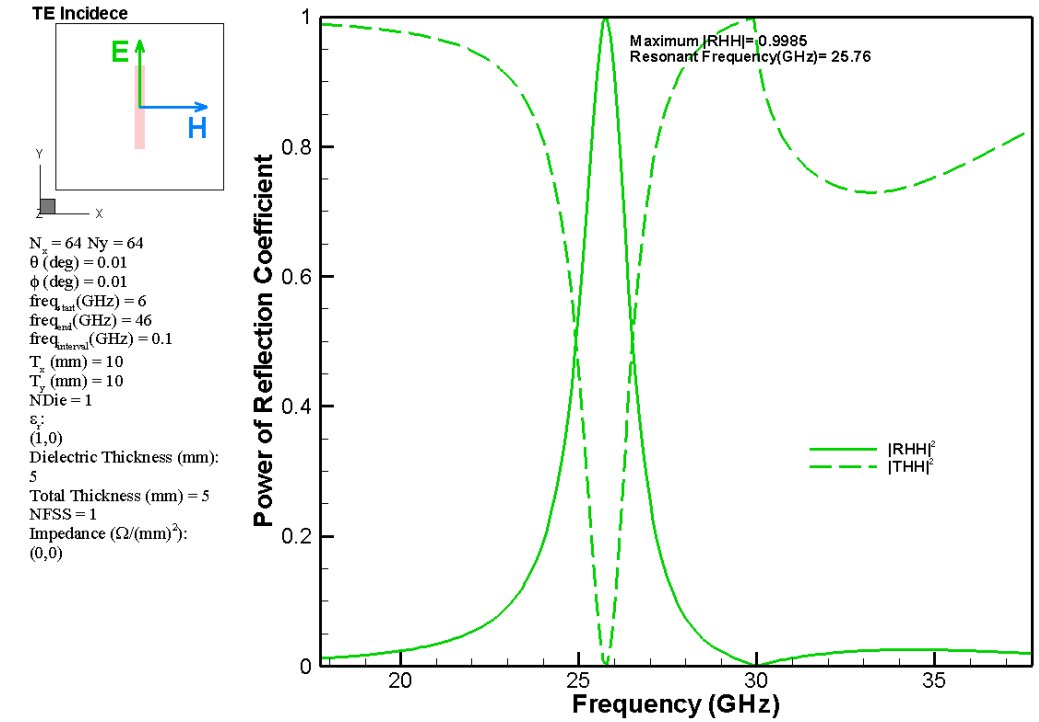

FIGURE 3-2 For dipole arrays, resonant frequency exist when E-field is parallel to length of dipole.

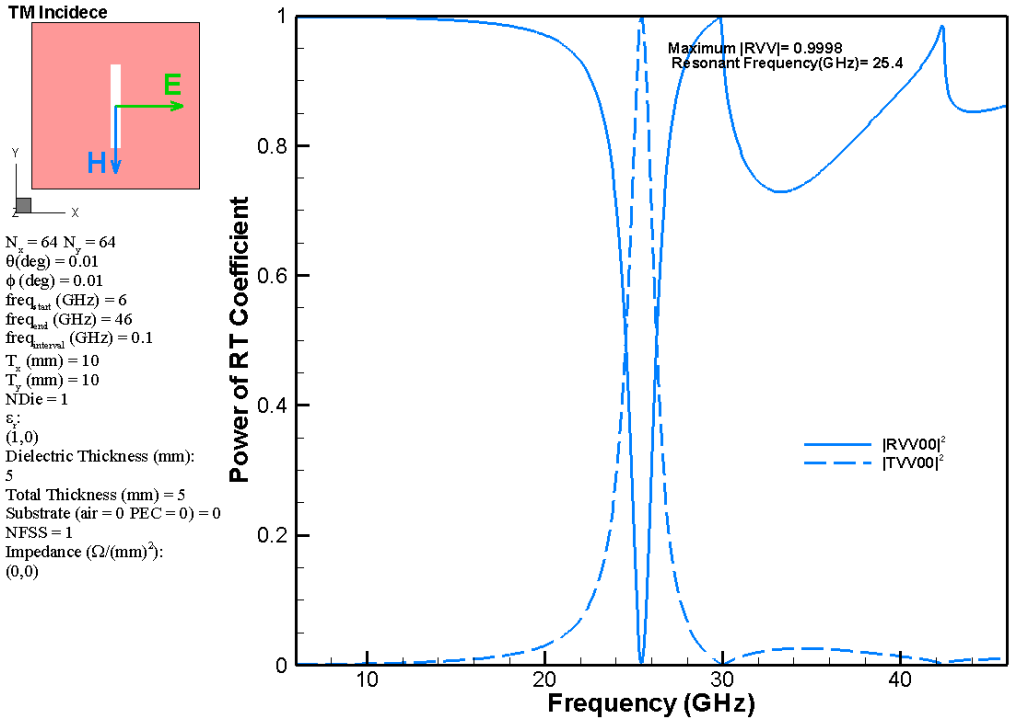

FIGURE 3-3 For slot arrays, resonant frequency exist when H-field is parallel to length of slot.

3.2 Dielectric Effect

3.2.1 Permittivity

For infinite extent dielectric, the resonant frequency f_0 of freestanding FSS will shift to lower frequency with the factor $\sqrt{\varepsilon_{eff}}$, where is the effective relative permittivity. The ε_{eff} is given by

Munk [8]

$$\varepsilon_{eff} = \begin{cases} \varepsilon_r & ,\text{case1} \\ (\varepsilon_r + 1)/2 & ,\text{case2} \end{cases} \tag{3.2}$$

where case one is that one dielectric on one side of the FSS, and the other case is that two dielectric with equal thickness and relative permittivity on both side of the FSS as illustrated in FIGURE 3-4. Eq.(3.2) is due to that ε_{eff} is the average of upper relative dielectric constant and lower relative dielectric constant.

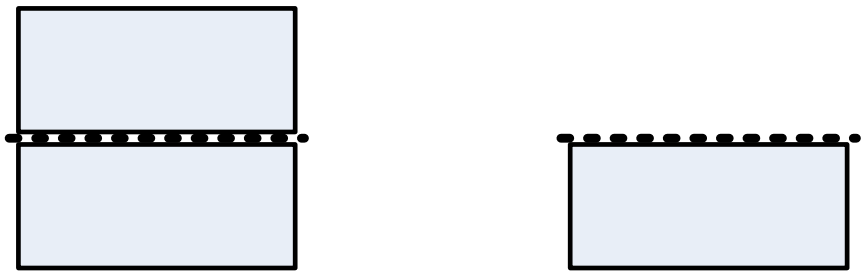

FIGURE 3-4 ***Left:***case1 ***Right:*** case2

FIGURE 3-5 illustrate that the resonant frequency will red shift if the relative dielectric constant increases.

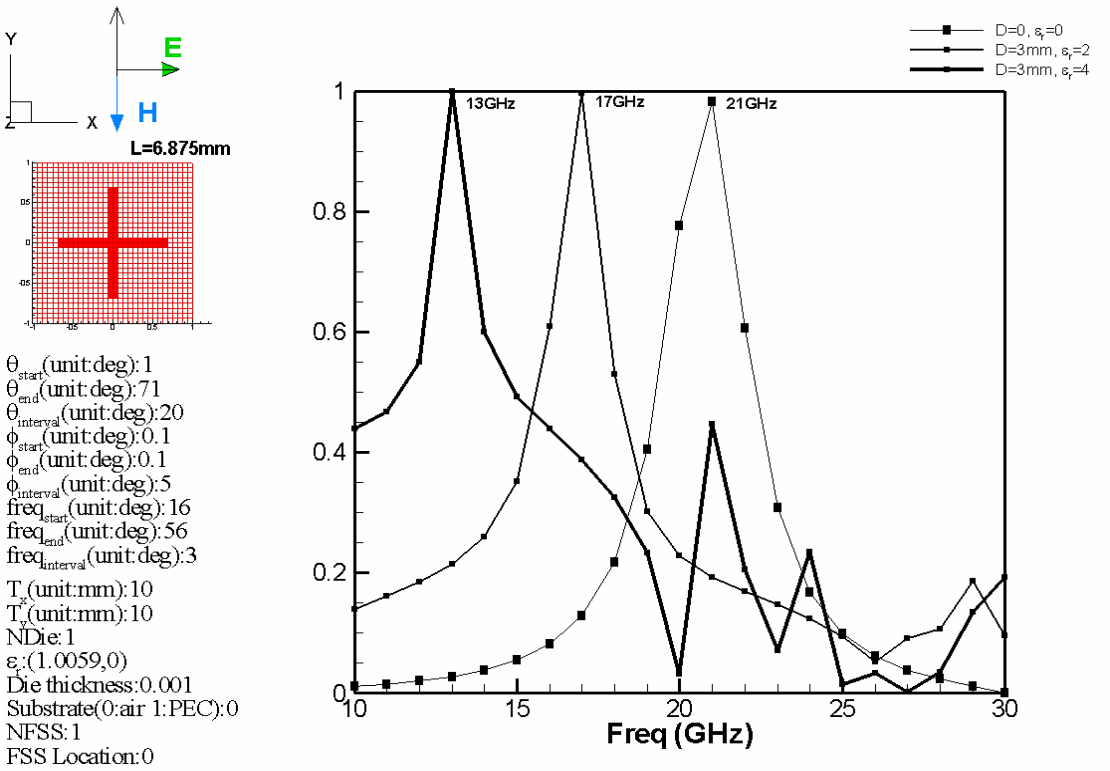

FIGURE 3-5 For infinite thickness dielectric, the resonant frequency shift to low frequency with increasing relative dielectric constant. This results is consistent with those obtained by Mittra in 1988[2].

3.2.2 Thickness

In previous section, the resonant frequency was $f_0/\sqrt{\varepsilon_{eff}}$,if the thickness of dielectric assumed infinitely extent. In this section we show that the resonant frequency was decreased with the increase in the thickness of the dielectric layer surrounding FSS as shown in FIGURE 3-6. But actually if the thickness of dielectric increase up to $0.05\lambda_r$ [8], where λ_r denotes the resonant wavelength of freestanding FSS, the resonant frequency have no significant decrease, and its value is approximately equal to $f_0/\sqrt{\varepsilon_{eff}}$.

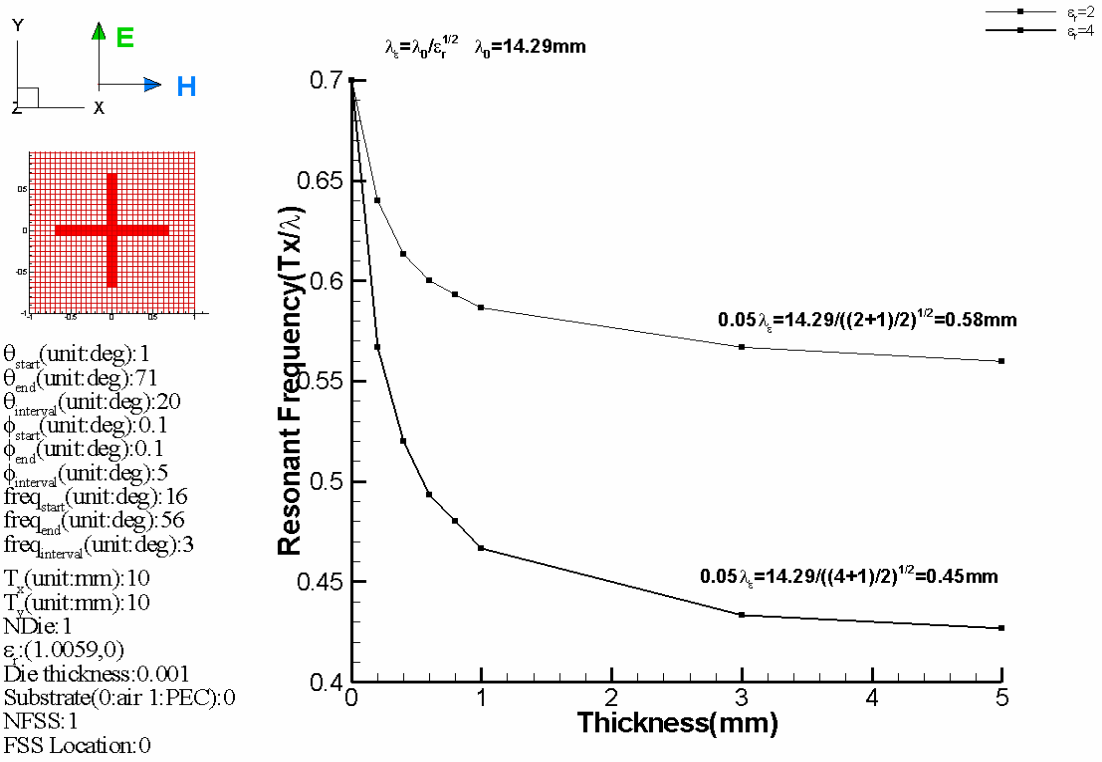

FIGURE 3-6 As the thickness of dielectric increases, the resonant frequency will decrease.

3.3 Lattice Constant (Periodic Spacing)

Lattice constant affects the bandwidth of an FSS. In general, the increase of lattice constant will decrease the bandwidth. However, Munk[8] shows some exception.

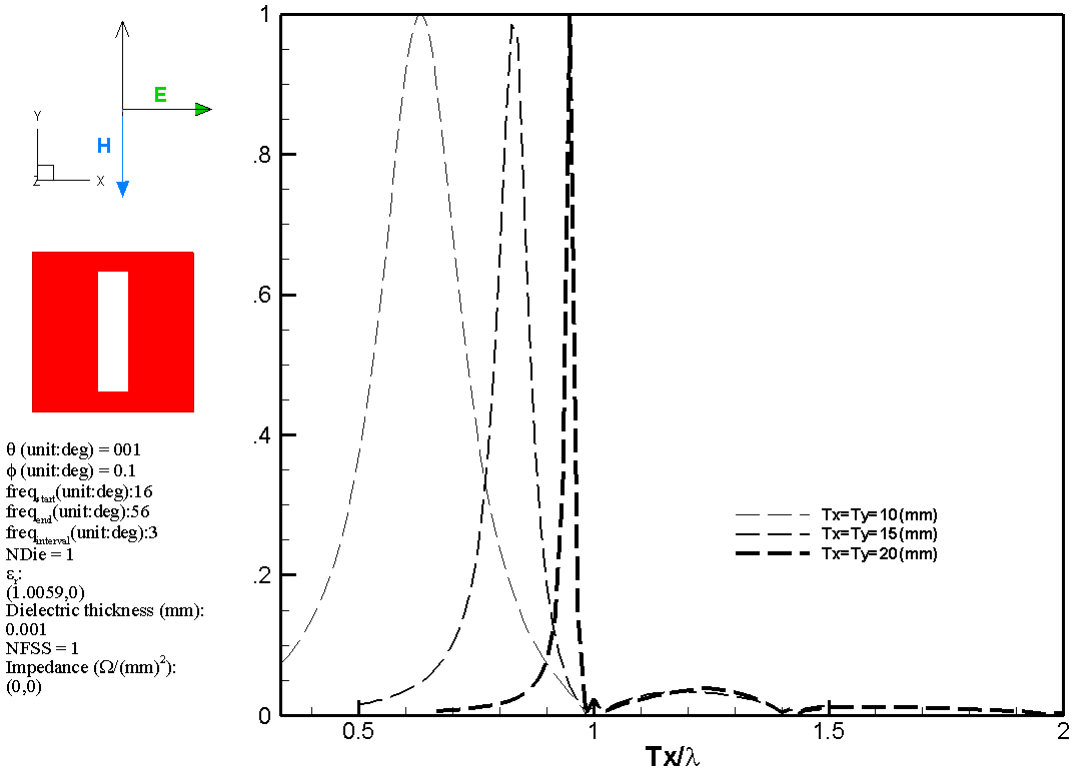

FIGURE 3-7 The bandwidth will increase as periodic spacing increases.

3.4 Wood's Anomalies

Wood's anomalies are that rapid variations in intensity in narrow spectrum as shown in FIGURE 3-8.They were first observed by Wood in the diffraction spectrum of optical gratings in 1902 and were termed anomalies since the effects could not be explained by ordinary grating theory [9]. Luebbers [10] has shown that Wood's anomalies are associated with a surface wave propagating the surface of FSS.

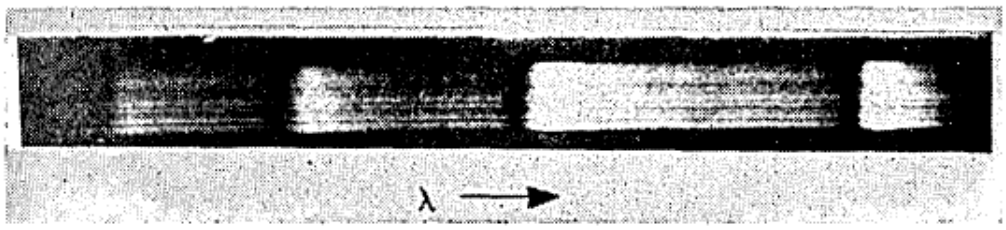

FIGURE 3-8 A Spectrum exhibiting Wood's anomalies[9]

For aperture-element FSS, Wood's anomalies denote the transmission null and usually occur near to or higher than the resonant frequency of periodic structure as illustrated in FIGURE 3-9. For circular aperture of rectangle grid arrays illuminated by normally incident field, the wavelength of Wood's anomalies λ_W can be obtained by [11]

$$\lambda_W = \left(\frac{\varepsilon_d}{m^2 + n^2} \right)^{\frac{1}{2}} D \qquad (3.3)$$

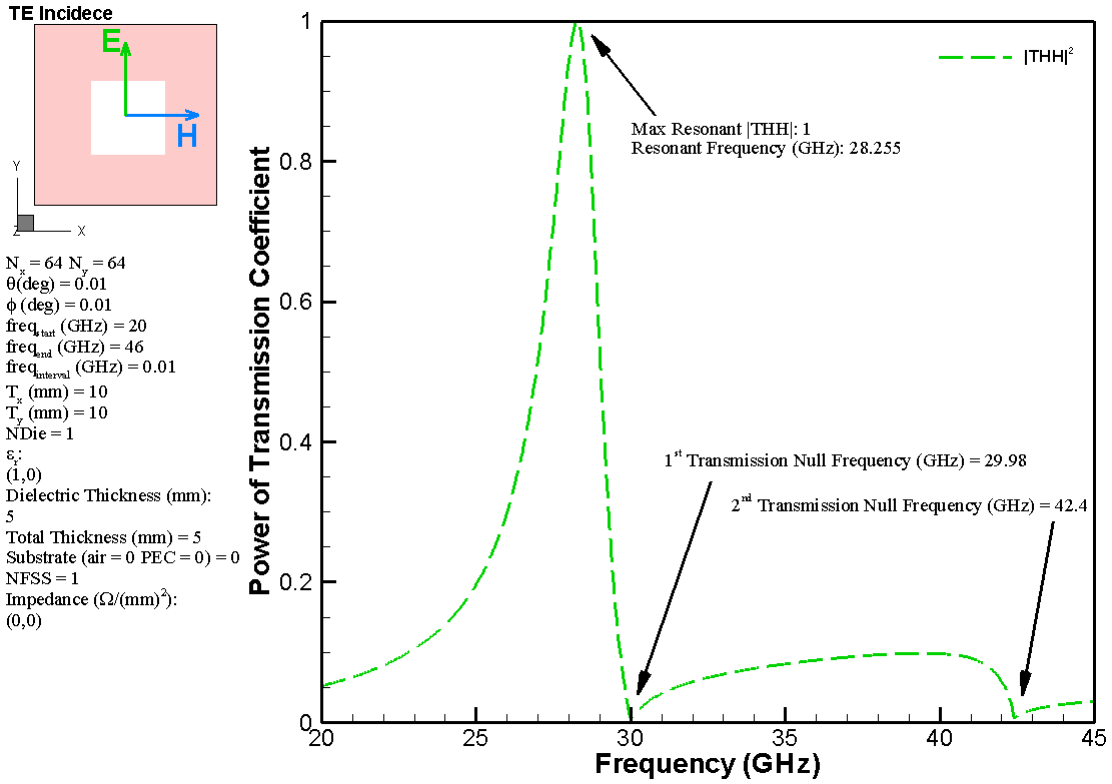

FIGURE 3-9 Two frequency of transmission null (Wood's anomalies) for freestanding square hole.

FIGURE 3-9 shows that first frequency of transmission null is 29.98 (GHz) and second frequency of transmission null is 42,4 (GHz) and compares to TABLE 3.1, first null is due to mode $(m,n) = (1,0)$ or $(0,1)$, and second null is due to mode $(m,n) = (1,1)$

m	n	λ_W (cm)	f_W (GHz)
0	1	1	30
0	2	0.5	60
0	3	0.333	90
1	1	0.707	42.426
1	2	0.447	67.082
1	3	0.316	94.868
2	2	0.353	84.853
2	3	0.277	108.167
3	3	0.2357	127.280

TABLE 3.1 shows that λ_W for (m,n) from 0 to 3**.**

3.5 Multi-Layered FSS

Single FSS without any dielectric have some disadvantages such that the resonant frequency and bandwidth depends on the incident angle and polarization. Thus, we design multi-layered FSS with dielectric loading to get a constant bandwidth and stable resonant frequency for angle of incidence and polarization. FIGURE 3-10 show Yee surface [12]which is three-layered frequency with patch-aperture-patch configuration. Yee surface have the stable bandpass characteristics for large scan angle. However, the bandwidth decreases with incident angle θ for TE polarization while the bandwidth increases with incident angle θ for TM polarization.

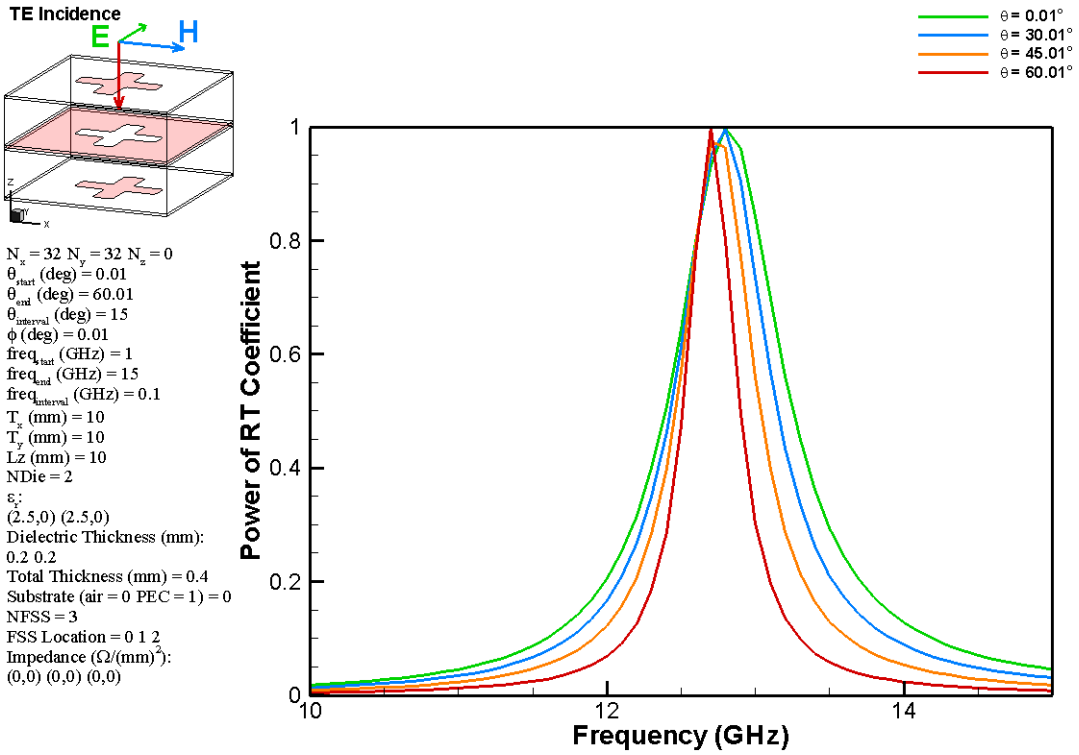

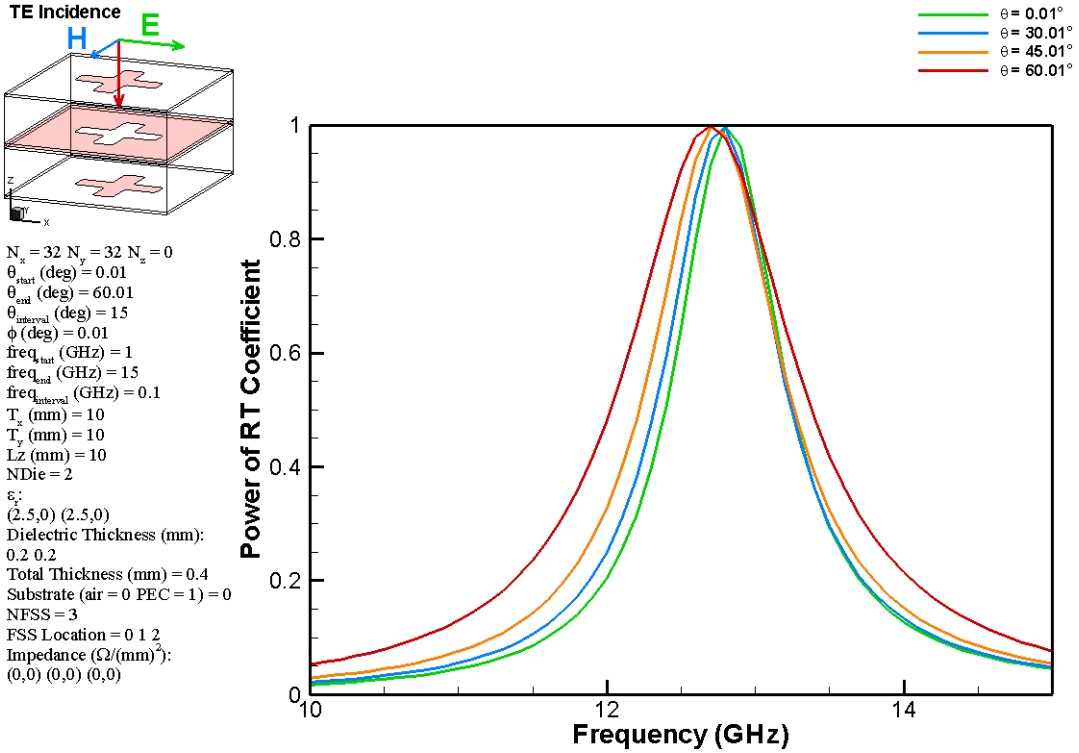

FIGURE 3-10 The FSS pattern is cross with patch-aperture-patch configuration, and the resonant frequency is 5.5 (GHz) for varying angle and different polarization.

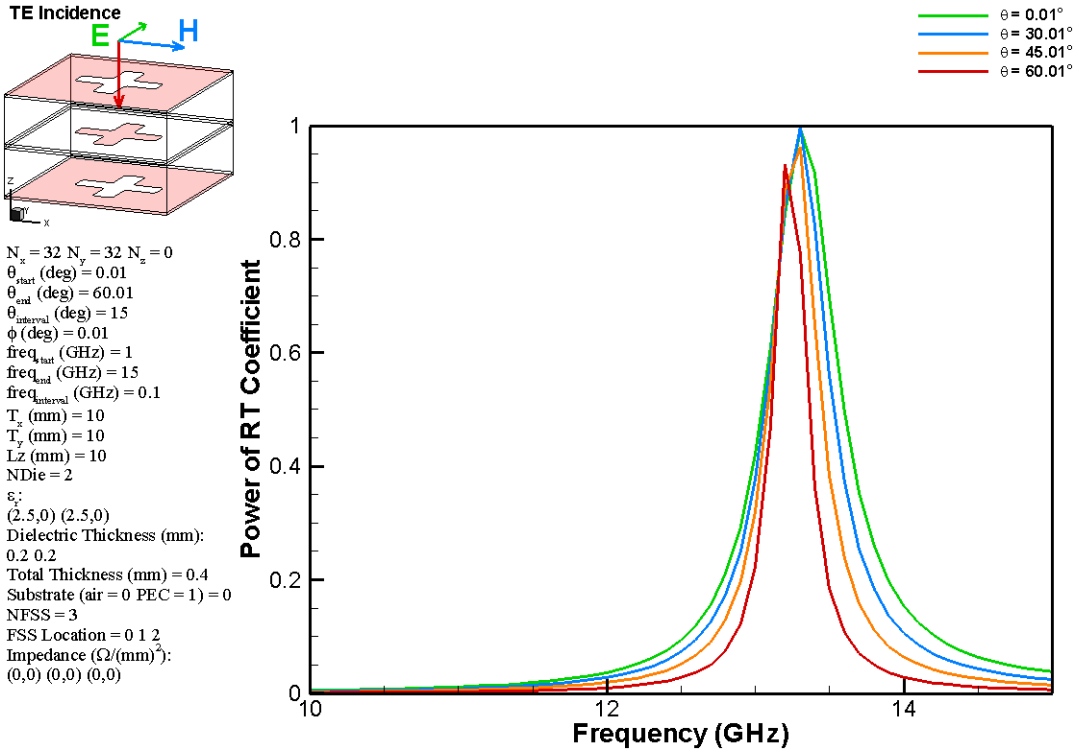

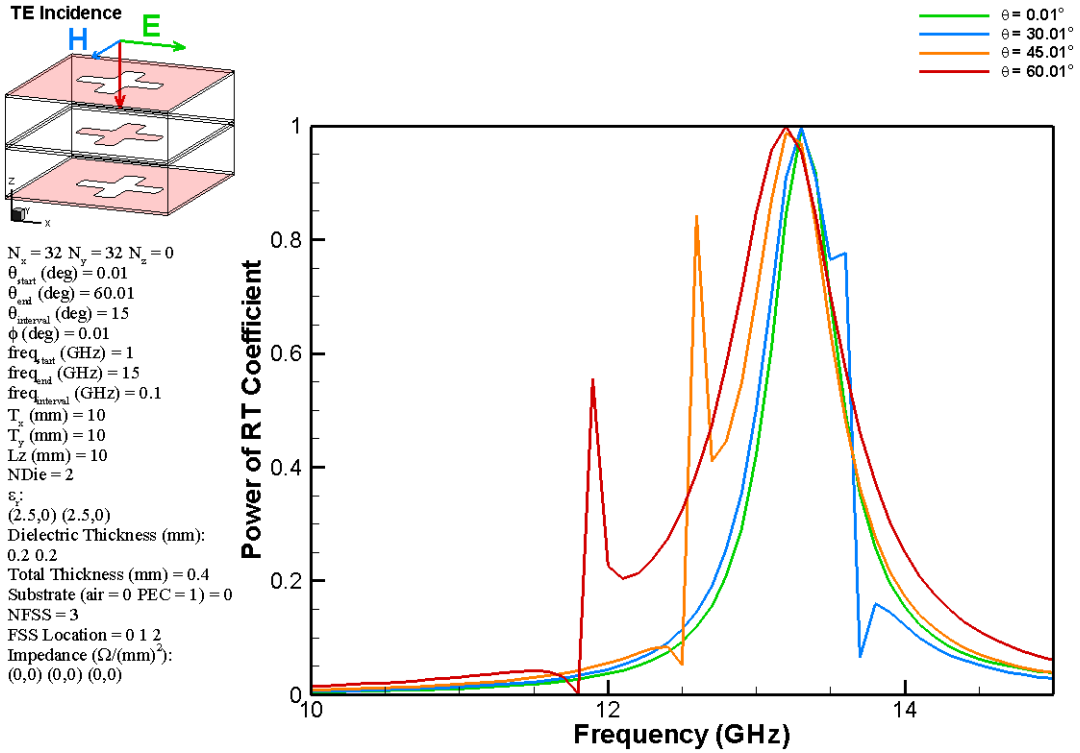

FIGURE 3-11 The FSS pattern is cross with patch-aperture-patch configuration

3.6 Resonances of Split Ring Elements

Recently, the split ring resonators (SRR) proposed by Pendry *et al.* [4] were shown to exhibit strong magnetic response to the incident field. In the long wavelength limit, the effective permeability of the SRR structure can be negative. Therefore, SRR serve as the key element for a left handed composite medium where the permeability and permittivity are simultaneously negative [13]. The mechanism responsible for the negative permeability of the SRR is the circulating current induced in the structure. As the current circulates in a manner such that the resultant magnetic field opposes against the incident one, the magnetization (magnetic polarization) becomes negative. This is attained when the frequency of the incident wave goes above the resonant frequency of the SRR structure, for the magnetic response begins to lag behind the incident field [14]. In view of this, FSS can also exhibit magnetic resonance in addition to electric one if the conducting currents circulate around the patch or aperture elements. In this section, we investigate the electric and magnetic resonances of FSS with the SRR elements. It is shown that two types of resonances occur for the SRR patch elements; one is

attributed to electric resonance and the other to magnetic resonance. Basically, the electric resonance can be attained as long as the incident electric field has a component parallel to the FSS plane, whereas the magnetic resonance can be achieved if the incident magnetic field has a component normal to the FSS plane, or the incident electric field has a component parallel to the ring edge with gap. In the latter case, the electric field can couple to the magnetic resonance through the ring gap. However, both resonances can produce gaps in the transmission spectra, around which the induced currents are enhanced to maximum values and the incident waves are hindered or even blocked.

For the electric type of resonance, the induced currents on the SRR elements oscillate in phase, giving rise to a strong reflection. Across the resonant frequency, the induced current switches its orientation. Due to symmetry of the current pattern, the net effect of magnetic response is negligible. For the magnetic type of resonance, the induced current circulates around the SRR element. In addition to enhancement of the induced current near the resonance, its circulating direction is reversed across the resonant frequency. A redshift of the resonant frequency with increasing the ring size, and a blueshift with increasing the gap size are observed. This is consistent with the characteristic of the equivalent *LC* circuit for the SRR element. In order to further evaluate the two types of resonances for FSS, the electric and magnetic dipole moments per unit cell are calculated. It is shown that the electric dipole moment attains the maximum value at the electric resonance, and the magnetic dipole moment changes signs across the magnetic resonant frequency. With the help of the expressions for the electric and magnetic dipole moments, coherent nature of the induced current for the electric resonance and circulating nature for the magnetic resonance are also revealed.

FIGURE 3-12 shows the schematic diagram of the SRR element for the FSS structure. In this study, we choose lattice constant a = 24 mm, l = 15 mm, w = 4:5 mm, and d = 3 mm. Denoting the surface current vector by $\mathbf{J}_s$, the electric and magnetic dipole moments are given as [15, 16]

$$\mathbf{p} = \frac{1}{jw}\int \mathbf{J}_s da \qquad (3.4)$$

$$\mathbf{m} = \frac{1}{2}\int \mathbf{r} \times \mathbf{J}_s da \tag{3.5}$$

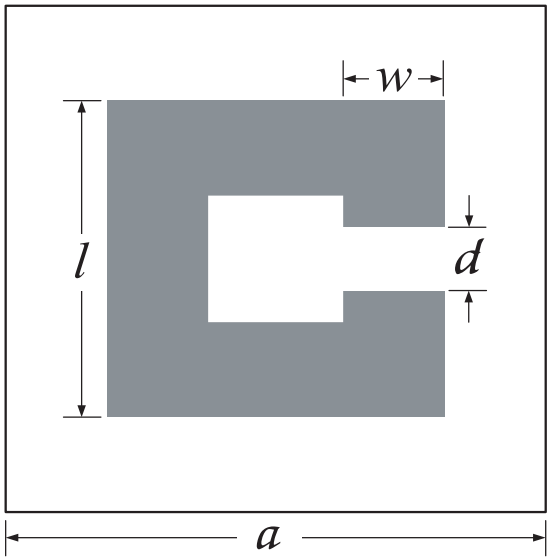

FIGURE 3-12 Schematic diagram of the SRR conducting element for the FSS structure.

3.6.1 Electric Resonance

The electric resonance of FSS can be attained as long as the incident electric field has a component along the FSS plane so that the induced currents on the conducting elements can couple and resonate with the incident wave. FIGURE 3-13 shows the transmitted power for TE incidence (the incident electric field lying completely in the FSS plane) with the incident electric field polarized normal to the ring edge with gap. For normal incidence ($\theta = 0^\circ$), the transmission dip appears at f = 10.7 GHz due to the electric resonance. Roughly speaking, the electric resonance occurs when the wavelength is approximately twice the element length ($\lambda = 2l$) [8] so that the resonant mode can reside on the structure. Accordingly, larger elements correspond to lower resonant frequencies, and smaller elements to higher resonant frequencies. For l = 15 mm, the electric resonance occurs at about f = 10 GHz, which is consistent with our result. Near the electric resonance, the induced current is enhanced to the maximum value, giving rise to a strong reflection. As a result, the corresponding transmission is reduced to minimum. FIGURE 3-14 shows the induced currents near the electric resonance for normal incidence at (a) f = 10.55 GHz and (b) 10.8 GHz. The induced current is basically oriented parallel or antiparallel to the polarization direction. Across the resonant frequency f = 10.7 GHz, the induced current switches

its orientation and the current strength is reduced away from the resonant frequency. This is manifest on the magnitude of the electric dipole moment $|\mathbf{p}|$, as shown in FIGURE 3-15. At the resonant frequency, the electric dipole moment attains the maximum value. This comes from the coherent oscillation of $\mathbf{J}_s$, as can be understood from Eq. (2). For oblique incidence (θ>0°), the resonant frequency may split into two ones, as seen in FIGURE 3-13. At larger incident angles, the frequencies of the two resonant modes separate more distantly from each other. For θ=30°, the electric resonances occur at f = 8.1 and 12.3 GHz, while for θ=60°, the electric resonances occur at f = 6:6 and 11.85 GHz. The degeneracy lifting comes from a phase delay of the incident wavefront between the edges of SRR element. The transmission dips of lower and higher frequencies correspond to symmetric and antisymmetric induced current patterns, respectively. For TE incidence with the incident electric field polarized parallel to the edge with gap, the electric resonances occur at about the same frequencies. FIGURE 3-17 shows the transmitted dips at f = 8:3 and 12.5 GHz for θ=30°, and f = 6:6 and 11.7 GHz for θ=60°. In this polarization, the transmission dips are sharper, and for larger oblique incidences the dip values are much larger than those in the other polarization (cf. FIGURE 3-13). However, if the incident electric field does not have components along the FSS plane, electric resonances may disappear.

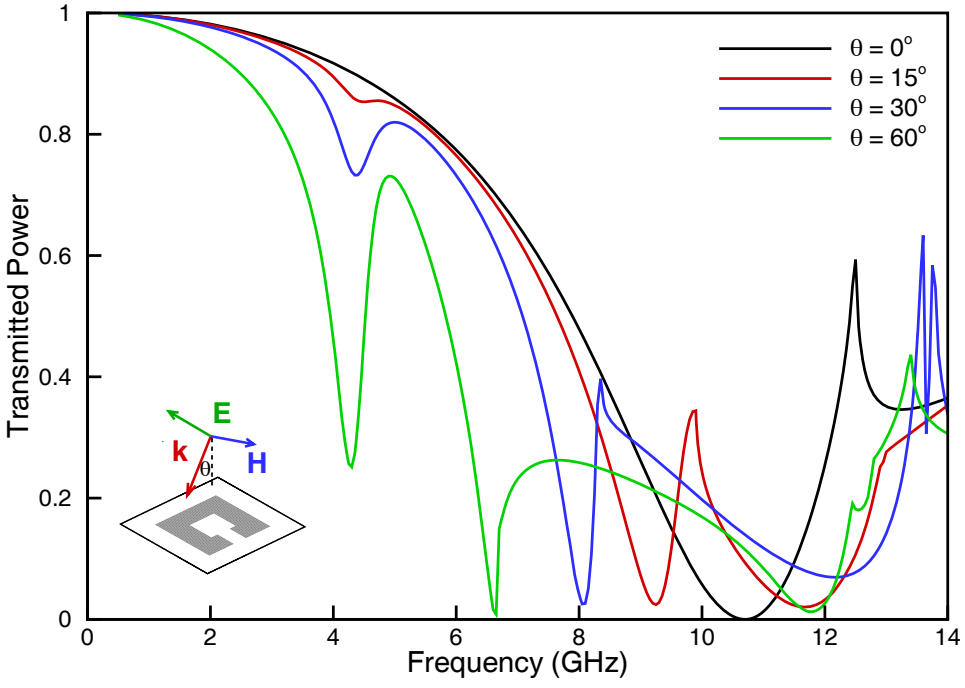

FIGURE 3-13 Transmitted power of the FSS with SRR elements for TE incidence with various incident angles. The incident electric field is polarized normal to the edge with gap.

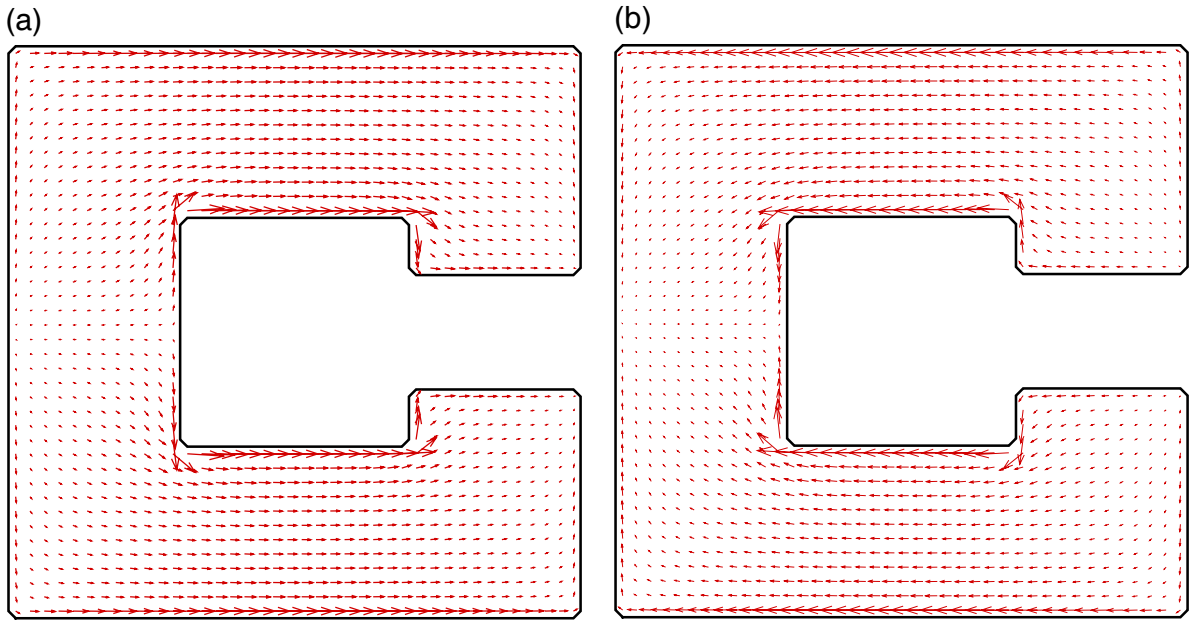

FIGURE 3-14 Surface currents of the FSS with SRR elements for normal incidence near the electric resonant frequency 10.7 GHz: upper figure at 10.55 GHz, and lower figure at 10.8 GHz. The incident electric field is polarized normal to the edge with gap.

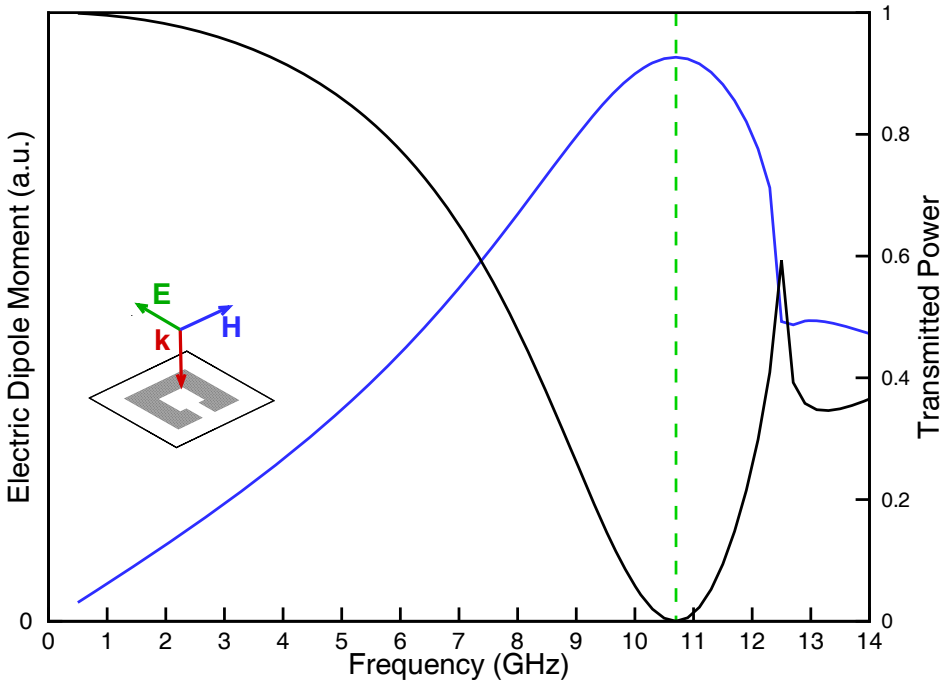

FIGURE 3-15 Electric dipole moment (blue line) and the transmitted power (black line) of the FSS with SRR elements for normal incidence. The dashed line denotes where the electric resonance occurs.

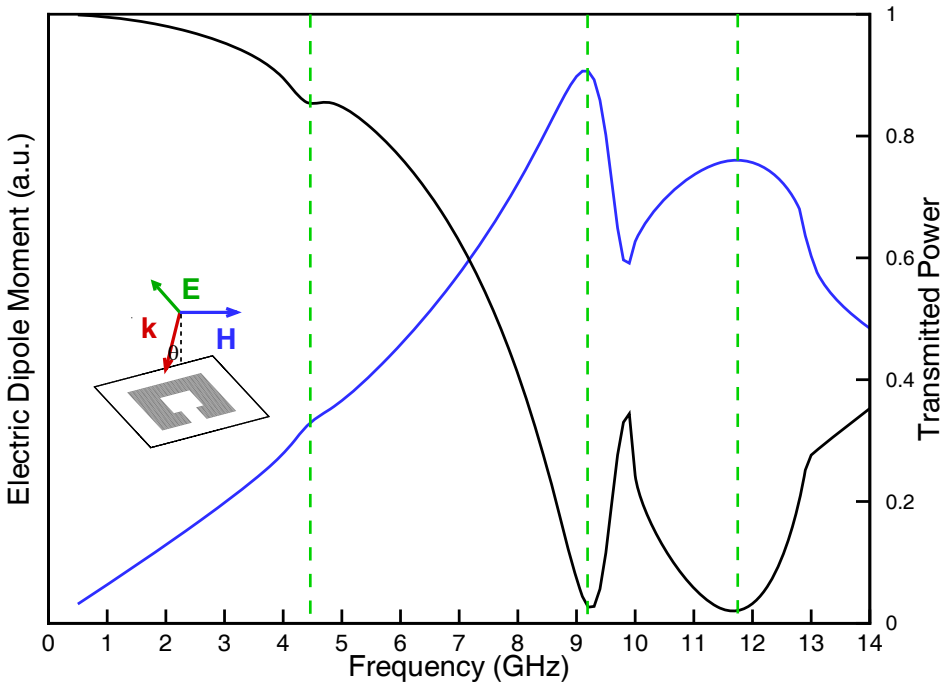

FIGURE 3-16 Electric dipole moment (blue line) and the transmitted power (black line) of the FSS with SRR elements for $\theta = 15^{\circ}$. The dashed line denotes where the electric resonance occurs.

FIGURE 3-18 shows the transmitted power for TM incidence (the incident magnetic field lies completely in the FSS plane). For higher oblique incident angles, the electric field becomes normal to the FSS plane, and the electric resonance gradually disappears. For θ=89° (the green line), the transmitted power is almost 1 except near the resonant frequency, where a very sharp transmission dip occur. In the limiting case of θ=90° (the dashed line), the transmitted power becomes unity.

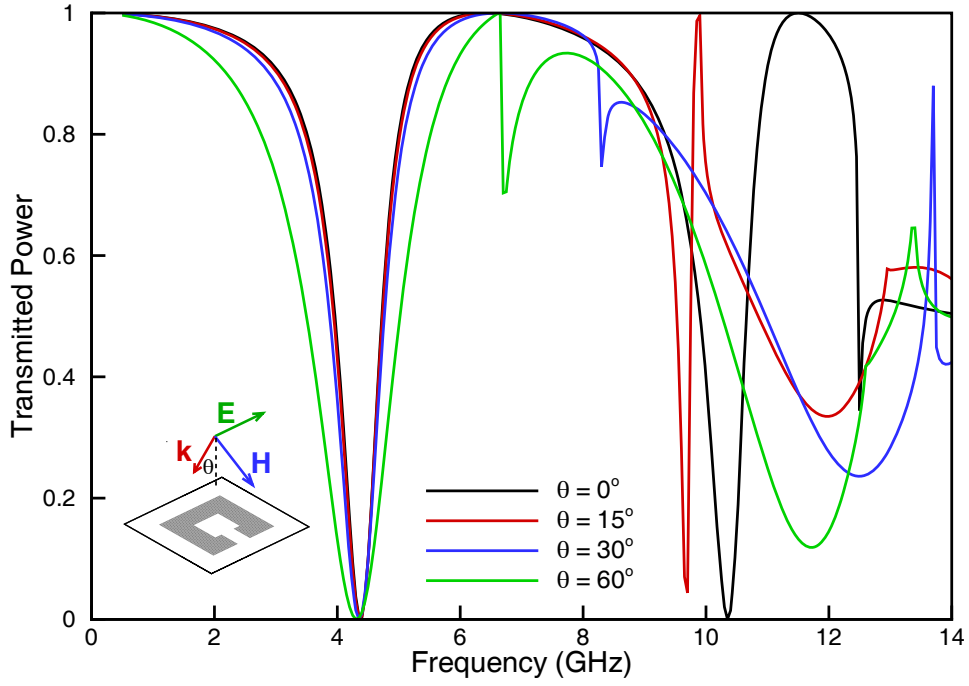

FIGURE 3-17 Transmitted power of the FSS with SRR elements for TE incidence with various incident angles. The incident electric field is polarized parallel to the edge with gap.

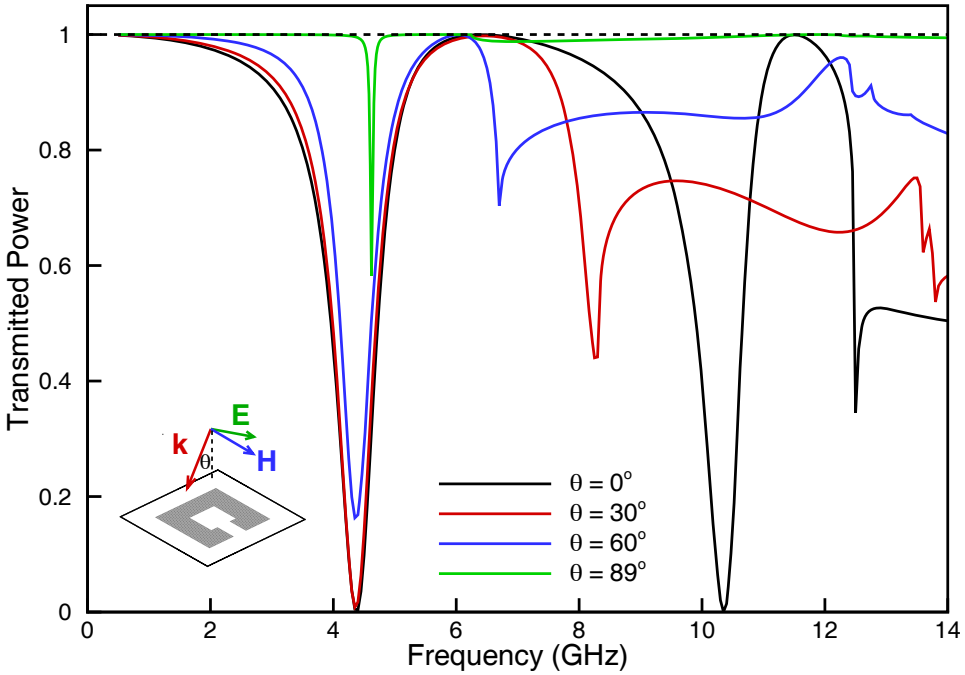

FIGURE 3-18 Transmitted power of the FSS with SRR elements for TM incidence with various incident angles. The incident magnetic field is polarized parallel to the edge with gap.

3.6.2 Magnetic Resonance

On the other hand, the magnetic resonance of FSS can be achieved only when the induced current circulates around the SRR element. In this case, the ring acts like an inductor and the gap like a capacitor. Therefore, the SRR element behaves as an *LC* resonator [4] provided that the current flows through the ring and gap in series connection. This is met by either of the two conditions: the incident magnetic field has a component normal to the FSS plane, or the incident electric field has a component across the gap [14, 17]. In either case, the displacement current in the gap can bridge the conducting current in the ring, and a circulating current is effectively formed. As in the case of electric resonance, transmission dips also occur near the magnetic resonance. In FIGURE 3-13, the incident electric field is polarized normal to the ring edge with gap. Therefore, the electric field does not couple to the magnetic resonance through the gap, and for normal incidence no magnetic resonances occur. While for oblique incidence, the magnetic field has a component normal to the FSS plane. The magnetic resonance gradually appears and the corresponding transmission goes down to minimum. This becomes more obvious for larger

incident angle θ. Note that magnetic resonances for different incident angles occur at the same frequency f = 4.35 GHz, around which the induced currents are enhanced and the incident waves are hindered to different degrees. Although the transmission dip feature is similar to the electric one, the mechanism of magnetic resonance is quite different. FIGURE 3-19 shows the induced currents near the magnetic resonance for various incident angles. As θ increases, the induced current on the lower edge changes its direction, and that on the left edge becomes stronger. As a result, a circulating current begins to take shape on the SRR element and the magnetic resonance gradually appears.

If the incident electric field is polarized parallel to the edge with gap, as shown in FIGURE 3-17, the magnetic resonance occurs for normal as well as oblique incidence. This is due to electric coupling to the magnetic resonance through the electric field across the ring gap. In this case, the incident waves are blocked at the resonant frequency with nearly null transmitted power. The magnetic resonance also accompanies with the sign change of the magnetic dipole moment given in Eq. (3.5). FIGURE 3-21 shows the magnetic dipole moment (3) for normal incidence. Across the resonant frequency, the real part of the magnetic dipole moment goes from positive to negative value, where the imaginary part reaches the minimum. In the meanwhile, the circulating current turns from counterclockwise to clockwise direction, as shown in FIGURE 3-22. In this regard, the effective magnetic permeability of the FSS structure can be negative if the magnetic resonance is strong enough. The magnetic resonant frequency f_0 is basically determined by the effective inductance L and capacitance C of the equivalent LC circuit for the SRR element, that is, $f_0 = 1 = 1/LC$. Figure ?? shows the transmitted power for various ring sizes. A redshift of f_0 with increasing the ring size l is observed. This is because the inductance L of the SRR is proportional to the area enclosed by the ring, and therefore a larger l corresponds to a lower f_0. For the same reason, a similar frequency shift can be found for a smaller ring width w (with the same ring size l), as shown in Fig. ??. In addition, the effect of the gap size on the transmitted power is shown in Fig. ??. A blueshift of f_0 with increasing the gap width d is observed, for C is inversely proportional to d, and larger d corresponds to higher f_0.

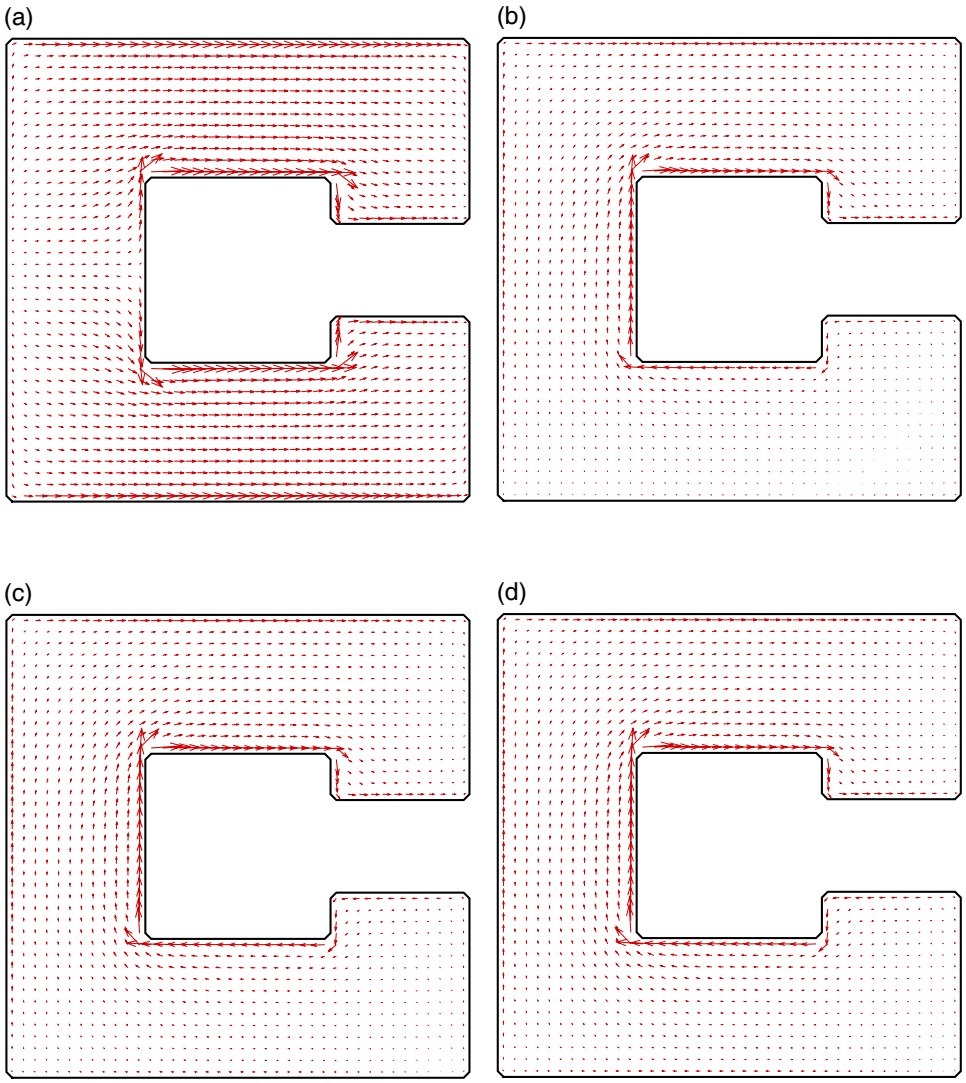

FIGURE 3-19 Induced currents of the FSS with SRR elements for TE incidence with the incident electric field polarized normal to the edge with gap. (a) $\theta = 0^\circ$, (b) $\theta = 15^\circ$, (c) $\theta = 45^\circ$, and (d) $\theta = 60^\circ$.

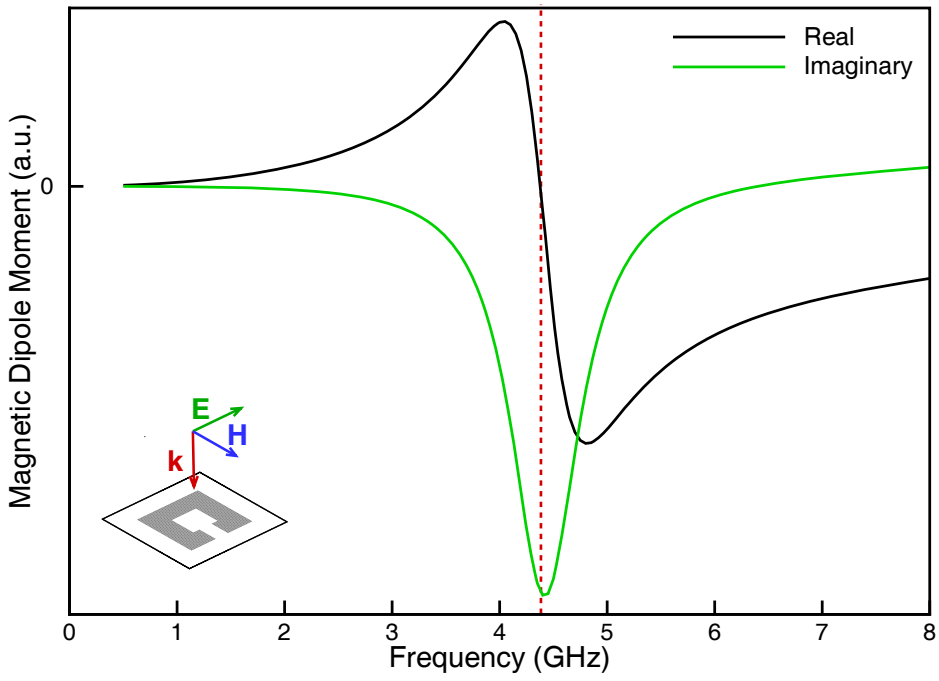

FIGURE 3-20 Magnetic dipole moment of the FSS with SRR elements for normal incidence.

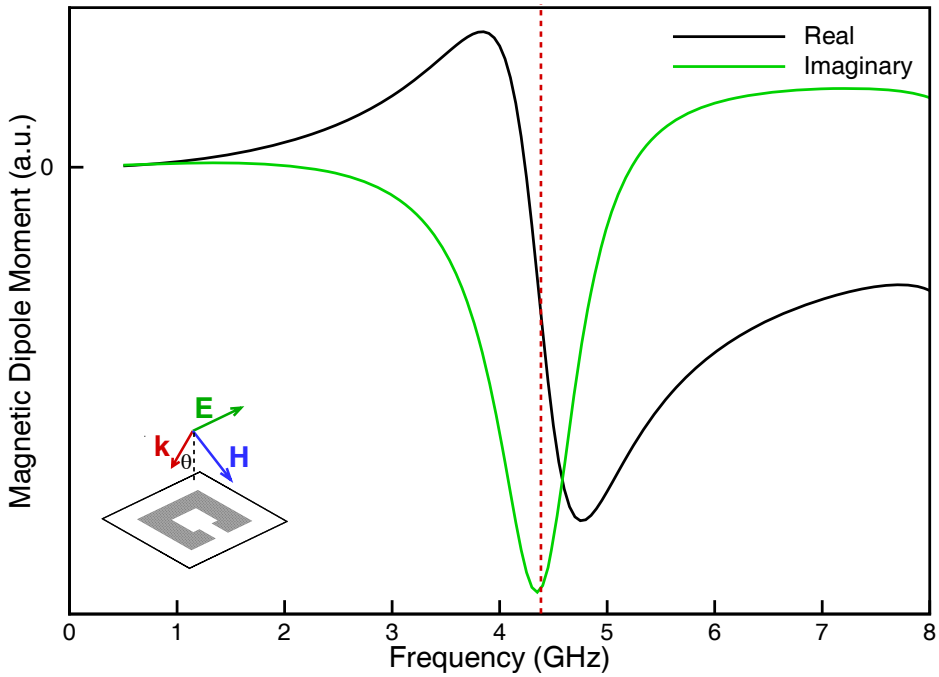

FIGURE 3-21 Magnetic dipole moment of the FSS with SRR elements at $\theta = 30^{\circ}$.

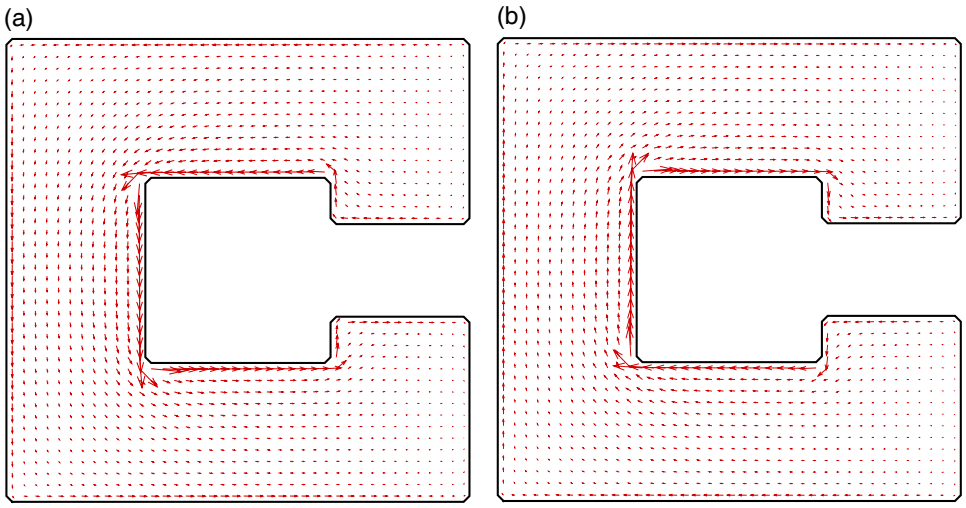

FIGURE 3-22 Surface currents of the FSS with SRR elements for normal incidence near the magnetic resonant frequency 4.35 GHz: upper figure at 4.3 GHz, and lower figure at 4.4 GHz. The incident electric field is polarized parallel to the edge with gap.

3.6.3 Multi-Layered SRR

For multilayered FSS, The effect of the number of layers on the transmitted power is shown in FIGURE 3-23 for normal incidence with the incident electric field polarized normal to the edge with gap. As the number of layers increases, the transmission dip splits and gradually expands. For five layers of FSS, a wide stop band with nearly null transmission is formed between 8.2 and

12.3 GHz. However, no stop band is observed if the incident electric field is polarized parallel to the edge with gap as shown in FIGURE 3-24. In this case, the electric resonances for different numbers of layers occur around 10.7 GHz. Meanwhile, the magnetic resonances appear exactly at 4.3 GHz.

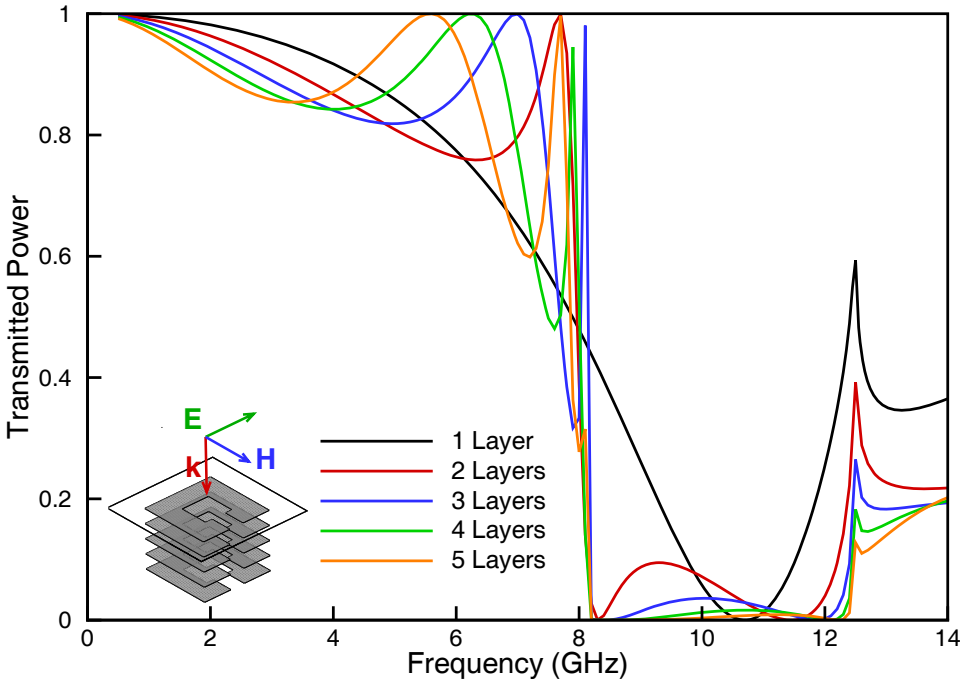

FIGURE 3-23 Transmitted power of the multilayered FSS with SRR elements for normal incidence with different numbers of layers. The incident electric field is polarized normal to the edge with gap.

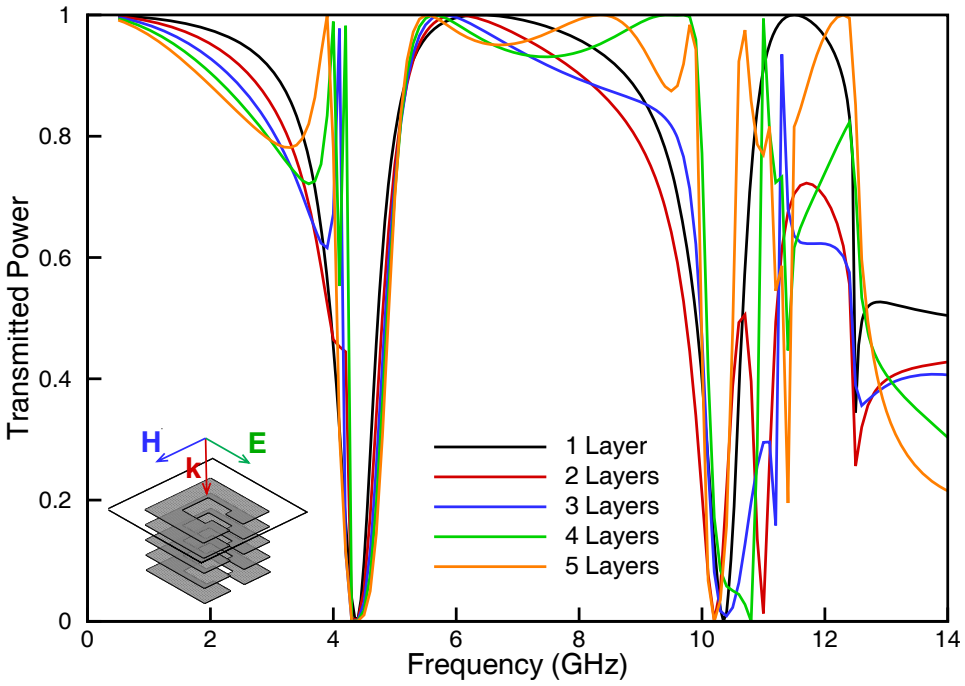

FIGURE 3-24 Transmitted power of the multilayered FSS with SRR elements for normal incidence with different numbers of layers. The incident electric field is polarized parallel to the edge with gap.

4 Concluding Remarks

Many design parameters of FSS, such as patch and aperture, thickness and permittivity of dielectrics, periodic spacing, and Wood's anomalies have been demonstrated how these parameters affect the reflection and transmission coefficient. Patch-type FSS exhibits bandstop behavior while aperture-type FSS exhibits bandpass property. For the FSS embedded in infinitely extent dielectric (typically 0.05λ), the resonant frequency will shift to lower frequency with factor is $\sqrt{\varepsilon_{eff}}$. For the thickness of dielectric between 0 and 0.05λ, the resonant frequency will be somewhere between f_0 and $f_0/\sqrt{\varepsilon_{eff}}$. The bandwidth decreases while lattice constant increases. We also presented Wood's anomalies which denote the transmission null here. Finally, we showed a multi-layered FSS called Yee-surface, which its resonant frequency does not be affected by polarization and incident angle.

metamaterials which exhibit novel electromagnetic properties not found in nature can be realized by FSS such as SRR. The SRR structure can be thought as LC resonant oscillator in circuit theory. We have shown the SRR pattern with different polarizations and incident angles. In transmitted power spectrum of SRR have two significant dips of SRR due to electric resonance and effective magnetic resonance though without magnetic material. We also h showed that electric and magnetic dipole moments of FRR at resonance frequencies have remarkable changes. The current density of SRR also changed its direction. Finally, we showed that multilayered SRRs that can increase the bandwidth at resonance peak.

5 References

[1] S. W. Lee, "Scattering by dielectric-loaded screen," *Antennas and Propagation, IEEE Transactions on [legacy, pre-1988]*, vol. 19, pp. 656-665, 1971.

[2] R. Mittra, C. H. Chan, and T. Cwik, "Techniques for analyzing frequency selective surfaces-a review," *Proceedings of the IEEE*, vol. 76, pp. 1593-1615, 1988.

[3] D. J. Kern, D. H. Werner, A. Monorchio, L. Lanuzza, and M. J. Wilhelm, "The design synthesis of multiband artificial magnetic conductors using high impedance frequency selective surfaces," *Antennas and Propagation, IEEE Transactions on*, vol. 53, pp. 8-17, 2005.

[4] J. B. Pendry, A. J. Holden, D. J. Robbins, and W. J. Stewart, "Magnetism from conductors and enhanced nonlinear phenomena," *Microwave Theory and Techniques, IEEE Transactions on*, vol. 47, pp. 2075-2084, 1999.

[5] M. Ohira, H. Deguchi, M. Tsuji, and H. Shigesawa, "Analysis of Frequency Selective Surface with Arbitrarily Shaped Element by Equivalent Circuit Model," *Electronics and Communications in Japan, Part 2*, vol. 88, 2005.

[6] T. Itoh, "Spectral Domain Immitance Approach for Dispersion Characteristics of Generalized Printed Transmission Lines," *Microwave Theory and Techniques, IEEE Transactions on*, vol. 28, pp. 733-736, 1980.

[7] S. T. Chase and R. D. Joseph, "Resonant array bandpass filters for the far infrared," *Applied Optics*, vol. 22, pp. 1774-1779, 1983.

[8] B. Munk, *Frequency selective surfaces*: John Wiley New York, 2000.

[9] A. Hessel and A. A. oliner, "A new theory of Wood's anomalies on optical gratings," *appl. opt.*, vol. 4(10), pp. 1275-1297, 1965.

[10] R. Luebbers and B. Munk, "Some effects of dielectric loading on periodic slot arrays," *Antennas and Propagation, IEEE Transactions on [legacy, pre-1988]*, vol. 26, pp. 536-542, 1978.

[11] S. H. Chang, S. Gray, and G. Schatz, "Surface plasmon generation and light transmission by isolated nanoholes and arrays of nanoholes in thin metal films," *Optics Express*, vol. 13, pp. 3150-3165, 2005.

[12] I. Tardy, C. H. Chan, and J. S. Yee, "Analysis of Yee frequency selective surface," *Antennas and Propagation Society International Symposium, 1991. AP-S. Digest*, pp. 196-199, 1991.

[13] D. R. Smith, W. J. Padilla, D. C. Vier, S. C. Nemat-Nasser, and S. Schultz, "Composite Medium with Simultaneously Negative Permeability and Permittivity," *Physical Review Letters*, vol. 84, pp. 4184, 2000.

[14] S. Linden, C. Enkrich, M. Wegener, J. Zhou, T. Koschny, and C. M. Soukoulis, "Magnetic Response of Metamaterials at 100 Terahertz," *Science*, vol. 306, pp. 1351-1353, 2004.

[15] D. J. Griffiths, *Introduction to Electrodynamics*, 3 ed: Prentice Hall, 1999.

[16] J. D. Jackson, "Classical Electrodynamics," 3 ed: Wiley, New York, 1999.

[17] N. Katsarakis, T. Koschny, M. Kafesaki, E. N. Economou, and C. M. Soukoulis, "Electric coupling to the magnetic resonance of split ring resonators," *Arxiv preprint cond-mat/0407369*, 2004.

出席國際學術會議心得報告

計畫編號	新型表面擇頻元件之設計：分析與計算(2/2)
計畫名稱	NSC 95-2221-E-002-220
出國人員姓名 服務機關及職稱	陳瑞琳 國立台灣大學應用力學研究所 助理教授
會議時間地點	2006 年 12 月 5 日至 7 日 新加坡
會議名稱	國際電漿及奈米科技應用研討會(International Workshop on Plasmonics and Applications in Nanotechnologies)
發表論文題目	Surface plasmon modes for photonic crystals of negative index materials

一、參加會議經過

本次會議 International Workshop on Plasmonics and Applications in Nanotechnologies 在新加坡 Grand Copthorne Waterfront Hotel 舉行，由新加坡國立大學(National University of Singapore)主辦，Data Storage Institute 公司協辦。會中邀請了數十位全世界在 Plasmonics 研究領域中知名的學者作學術報告。會議進行有口頭報告及海報張貼兩種方式，所有口頭報告皆為大會的邀請演講，與會其他人員則以海報型式報告其研究內容。

本次會議約有十數國共一百餘人參加，其中來自台灣的學著約有十數位，包括台灣大學物理系蔡定平教授、光電所楊志忠教授、師範大學物理系劉威志教授、成功大學光電所藍永強教授，及海洋大學光電所江海邦教授等。我們於 4 日下午搭華航班機直達新加坡，然後下塌 Grand Copthorne Waterfront Hotel。當天晚上大會並且準備了 Reception dinner。5 日早上八點三十分開始進入議程，會期為期三天。

會議第一天(12 月 5 日)有四個 session，分別是 Plasmonics Opening，Planar Surface Plasmon Polariton Structures，Metamaterials 及 Applications in Biotechnology。演講者包括 Polman，Atwaten，Brongersma，Stockman，Shalaev 等知名學者，特別的是，在四十年前提出負折射概念的 Veselago 也被邀請到會中報告。當天的演講者幾乎都有 Nature，Science 及 Physical Review Letters 等級的發表論文。其中，Polman 綜合整理了表面包漿的生成、傳播及偵測。Atwater 提出如何在奈米度使用 Plasmonics 來製造光波元件。Stockman 提出如何控制奈米尺度的光場。Shalaev 則致力於在光波尺度製造負折射物質，並將其耗散降低。當天晚上大會並且準備了 Banquet dinner。

會議第二天(12 月 6 日)也有四個 session，分別是 Active Plasmonic Structures and Nanodevices，Plasmon-Polaritons and Ultramicroscopy、Optical Recording 及 Plasmonic Nanostructures: Holes and Ridged Apertures。演講者包括 Dereux，Martin-Moreno，Zayats，Tominaga 及蔡定平教授等人。其中 Dereux 提出如何讓表面電將轉向，Martin-Moreno 報告的內容為金屬孔洞結構的表面電漿散射，Zayats 報

告的內容則為表面電漿子週期結構的光學特性及其應用。Tominaga 則在光儲存中表面電漿的角色提出新的看法。蔡教授在奈米尺寸的光儲存影像及蝕刻技術提出報告。海報論文的張貼在下午進行，共有四十一份論文，其中約有十多份來自台灣的學者。本人的論文題目為”Surface Plasmon modes for photonic crystals of negative index materials”

會議第三天(12 月 7 日)有四個 session 分別是 Plasmons, Phonons and Lasers，Plasmons, Polaritons and Excitons，Plasmons and Polaritons 及 Applications。演講者包括 Martin，Garcia-Vidal 及 Quidant 等人。其中 Martin 提出 Plasmonic 天線的研究，Garcia-Vida 則解釋光如何穿過次波長孔洞結構。Quidant 則談到在微米及奈米尺度下表面電漿的操控。由於我只預備停留四天三夜，在參加完早上的議程後便在下午從新加坡搭機於晚上回到台北。

二、與會心得

此次會議主辦單位邀請了在 Plasmonics 研究領域中，全世界知名並且具有領導者地位的數十位傑出學者齊聚一堂，討論當前 Plasmonics 研究最重要的課題、待解決的問題及未來的研究方向。不論是在光波元件的應用、表面電漿特性的探討，乃至負折射物質的實作都是當前 Plasmonics 領域的研究焦點。

本人在此次會議中獲得了許多寶貴的知識，對於日後的研究工作甚有助益。Plasmonics 的研究在科學及科技領域的重要性日益增加，特別是有關金屬奈米結構(metallic nanostructures)的光學問題，或簡稱奈米光學(nano-optics)，包括表面電漿的激發、次波長孔洞結構的異常穿透現象，奈米金屬顆粒或叢集的光學特性，表面電漿在結構表面的傳播行為，超小尺度的波導，高效率感測器及積體光波元件等。本人未來將繼續在 Plasmonics 研究工作上繼續努力。

此次研討會全部為大會邀請演講，此類會議的學術性質比一般同時進行的會議為高。參加者可以在同一時間內聽到多位學者對相近議題的討論。國內學者可以考慮多參加此類會議，利用機會與國外學者交流，並於會後在國內密集討論，期能有豐碩的收穫，以利日後研究的進行。

攜回之資料及文件：

大會論文全文光碟片及論文摘要集紙本。